ACS APPLIED NANO MATERIALS

www.acsanm.org Article

Role of Oxidation–Reduction Dynamics in the Application of Cu/ZnO-Based Catalysts

Robert Gleißner, Simon Chung, Guilherme D. L. Semione, Leon Jacobse, Michael Wagstaffe, Steffen Tober, A. Joanne Neumann, Gökhan Gizer, Christopher M. Goodwin, Markus Soldemo, Mikhail Shipilin, Patrick Lömker, Christoph Schlueter, Olof Gutowski, Matthias Muntwiler, Peter Amann, Heshmat Noei, Vedran Vonk, and Andreas Stierle*

Cite This: *ACS Appl. Nano Mater.* 2023, 6, 8004–8016 Read Online

ACCESS | Metrics & More | Article Recommendations | Supporting Information

ABSTRACT: We investigated Cu nanoparticles (NPs) on vicinal and basal ZnO supports to obtain an atomistic picture of the catalyst's structure under *in situ* oxidizing and reducing conditions. The Cu/ZnO model catalysts were investigated at elevated gas pressures by high energy grazing incidence X-ray diffraction and ambient pressure X-ray photoelectron spectroscopy (AP-XPS). We find that the Cu nanoparticles are fully oxidized to Cu_2O under atmospheric conditions at room temperature. As the nanoparticles swell during oxidation, they maintain their epitaxy on basal ZnO (000 ± 1) surfaces, whereas on the vicinal ZnO ($10\bar{1}4$) surface, the nanoparticles undergo a coherent tilt. We find that the oxidation process is fully reversible under H_2 flow at 500 K, resulting in predominantly well-aligned nanoparticles on the basal surfaces, whereas the orientation of Cu NPs on vicinal ZnO was only partially restored. The analysis of the substrate crystal truncation rods evidences the stability of basal ZnO surfaces under all gas conditions. No Cu–Zn bulk alloy formation is observed. Under CO_2 flow, no diffraction signal from the nanoparticles is detected, pointing to their completely disordered state. The AP-XPS results are in line with the formation of CuO. Scanning electron microscopy images show that massive mass transport has set in, leading to the formation of larger agglomerates.

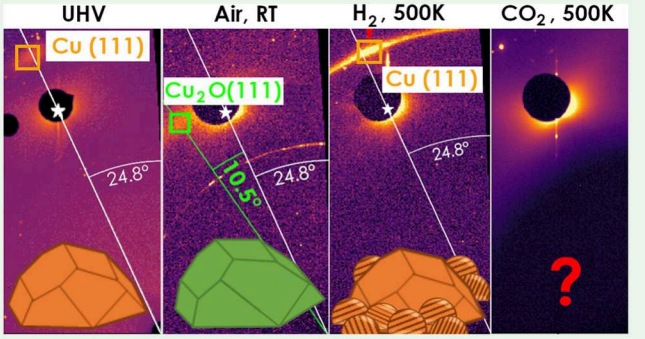

KEYWORDS: *Cu/ZnO, methanol, model catalyst, vicinal, active sites, in situ, ambient pressure*

INTRODUCTION

Cu/ZnO-based catalysts are utilized for CO_2 hydrogenation to methanol,[1] methanol steam reforming,[2,3] and the low-temperature water-gas shift reaction[4] and are researched for their application in methanol dehydrogenation to formaldehyde[5] and methyl formate.[6] The research of this specific and similar catalytic systems is followed with high attention because the implementation of closed carbon loops is envisioned as an important pillar to reduce anthropogenic CO_2 emissions.[7,8]

In heterogeneous catalysis, the Cu/ZnO system also serves as a precedential case study to explore the cause of strong metal–support interactions (SMSI),[1] in which both Cu and ZnO play an intertwined role during the reaction. At the center of a decade-long debate on methanol synthesis over Cu/ZnO-based catalysts is the nature of the active reaction sites.[1,9−14]

Methanol synthesis can be achieved from both CO and CO_2;[15−18] however, mixtures of $H_2/CO/CO_2$ show the highest performance over nanosized Cu/ZnO-based catalysts. Isotope labeling experiments show that CO_2 is the main source of carbon for the synthesis of methanol over Cu/ZnO-based catalysts.[17,18] H_2 is needed for the hydrogenation process and acts as a reducing agent to the catalyst. The CO content in the mixture withdraws the water that is generated as a byproduct, thus inhibiting the back-reaction from methanol to CO_2 and H_2, while also acting as a reducing agent to the catalyst. CO_2 acts as both oxidizing and reducing agent, as the conversion to methanol requires CO_2 to dissociate into CO and O species. The migration of Zn atoms onto Cu nanoparticles (NPs) under reducing conditions was reported in different experiments, forming metallic[9] or partially positively charged[11] Zn decorations as well as graphitic-like[12] or wurtzite[14,19] ZnO structures upon reoxidation. In addition to Zn migration, low-coordinated Cu atoms are suspected to be a prerequisite for high performance during catalysis.[11,20−22] Planar defects and lattice strain are also reported to play a particular role in the

Received: March 24, 2023
Accepted: April 21, 2023
Published: May 3, 2023

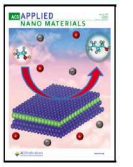

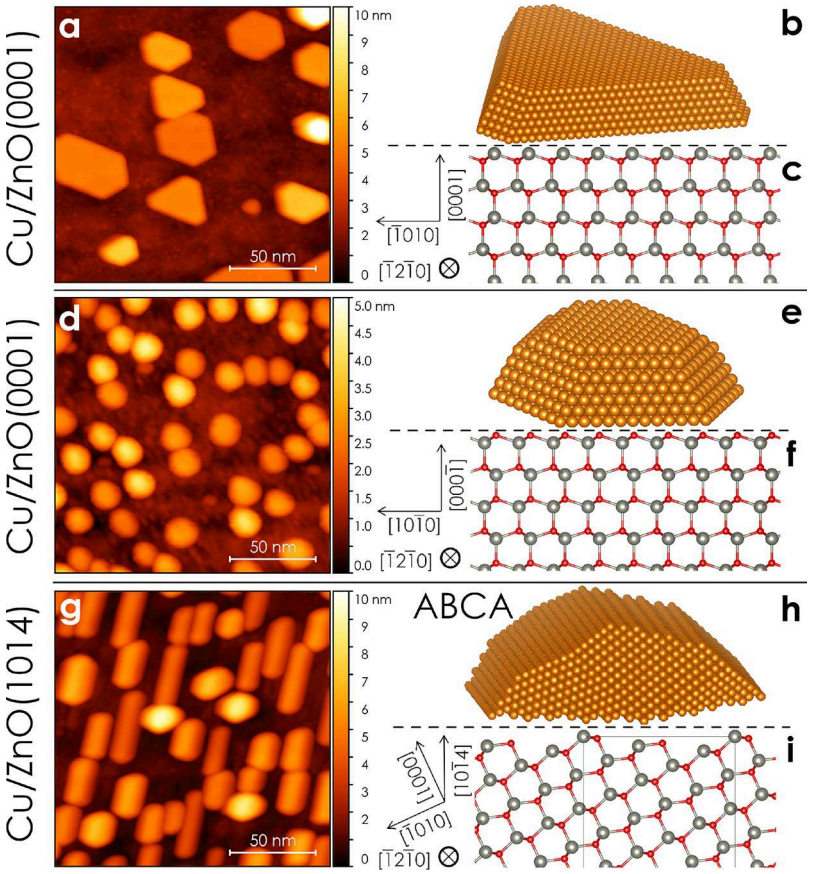

Figure 1. Effect of the ZnO substrate on the Cu particle morphology for equal UHV preparation conditions via thermal Cu evaporation. (a, d, g) STM images obtained at V_{gap} = 1.5−2.0 V and I_T = 0.1−0.5 nA.[25] (b, e, h) Schemes of prevalent Cu NPs on the respective ZnO surface. Note that for (h) only a particle with ABCA stacking is shown. (c, f, i) Cross sections of the ZnO surfaces.

catalytic performance of these nanosized crystals.[21,23] The catalyst's structural changes together with sintering and agglomeration effects during oxidation−reduction processes thus became a focal point in the controversy of the nature and cycle stability of the active reaction sites.

Commercial Cu/ZnO-based powder catalysts feature a mixture of NP facets and facet interactions. In 2013, Zheng et al.[24] showed the formation of vicinal ZnO(10$\bar{1}$4) facets from a ZnO(0001) single crystal surface. Despite its stepped nature, these facets were found to be very stable under UHV conditions. Their presence and the resulting consequences for the application of Cu/ZnO-based catalysts were overseen in the decade-long debate concerning the catalyst's active sites.

In our earlier study,[25] we investigated the morphology of Cu NPs grown on basal ZnO(0001), ZnO(000$\bar{1}$), and vicinal ZnO(10$\bar{1}$4) single crystals under UHV conditions. In brief, (i) Cu NPs on ZnO(0001) show a bimodal growth with flat hexagonal islands (H = 3.9 nm, D = 27.1 nm) and smaller tetrahedral NPs (H = 7.1 nm, D = 14.5 nm,) which both are (111) oriented; (ii) Cu NPs on ZnO(000$\bar{1}$) are round (H = 2.4 nm, D = 9.0 nm) and also show a (111) orientation; (iii) Cu NPs on ZnO(10$\bar{1}$4) are elongated parallel to the surface steps (about H = 5 nm, D = 10 nm, L = 50 nm) and show a 25.6° tilt to align the Cu(111) planes parallel to the (0001) planes of the ZnO(10$\bar{1}$4) substrate. This results in the formation of Cu NPs with an 85:15 ratio of ABCA and ACBA stacking of (111) layers and a morphology that presents large facets of densely spaced Cu surface steps (Figure 1). These facets thus expose low-coordinated Cu sites that are suspected to be beneficial for the catalytic performance during methanol synthesis,[11] which is seen as one explanation for the decrease in activity for methanol synthesis for NP sizes below 8 nm.[26] It is of great importance to investigate the behavior of densely stepped Cu NPs at the relevant temperatures and pressures under reducing and oxidizing atmospheres to garner insight into the stability of these low coordinated sites.

Generally, Cu NPs show lower kinetic barriers for oxidation in comparison to bulk Cu as the oxidation rate depends on $P_{O_2}^{1/n}$ with $n \geq 4$ for Cu bulk[27] and $n \approx 1.5$ for Cu NPs.[28] At room temperature, Cu NPs oxidize in a two-stage process, first linear and then with a direct-logarithmic rate law. The oxidation process is thus self-limited to an oxide layer of 2 nm thickness.[28] In contrast, single-[29] or polycrystalline[30] Cu shows an inverse-logarithmic oxidation rate. The onset of the formation of the monoclinic CuO phase under ambient temperature and air pressure is expected to occur after weeks or even months of native oxidation.[31,32]

In this study, we investigate the oxidation and reduction behavior of Cu NPs on Zn-terminated ZnO(0001), O-terminated ZnO(000$\bar{1}$), and vicinal ZnO(10$\bar{1}$4) (termed Zn-bZnO, O-bZnO, and vZnO in the following). This comparison provides direct insight into the differences in the oxidation and reduction mechanisms dependent on the NPs facets, which are directly influenced by the ZnO substrate's termination.[25,33,34] We employ a multitude of methods, such as *in situ* ambient pressure high energy grazing incidence X-ray diffraction (HE-GIXRD), X-ray reflectometry (XRR), UHV and ambient

https://doi.org/10.1021/acsanm.3c01306
ACS Appl. Nano Mater. 2023, 6, 8004−8016

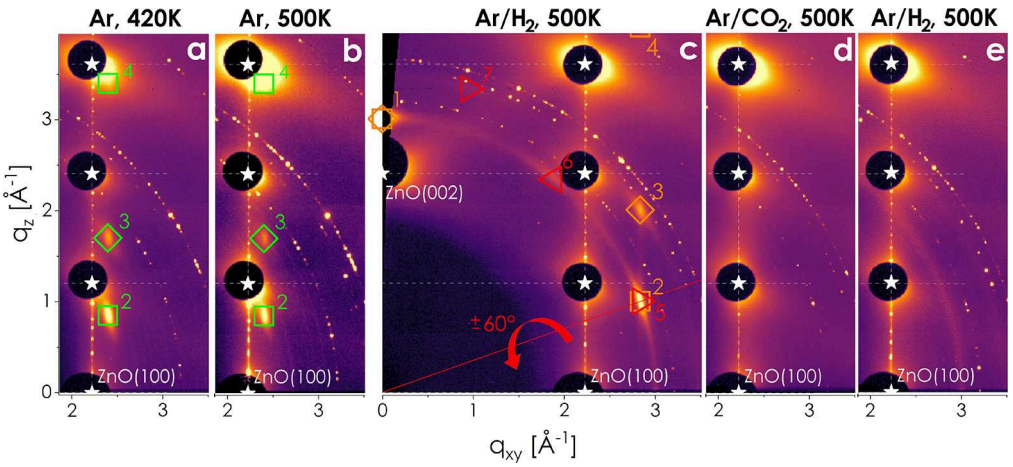

Figure 2. H−L maps of the NPs on Zn-bZnO. (a) After native oxidation. (b) After increasing the temperature to 500 K. (c) After reduction. (d) After oxidation. (e) After rereduction. Gas feeds: 1 bar, 100 mL/min, (4:1) ratio of mixtures if applicable. Symbols represent Bragg peaks while their orientation emphasizes the stacking order (ABCA or ACBA): ZnO (white stars), Cu_2O NPs (green squares), and Cu NPs (orange squares) with (1) (111), (2) $(11\bar{1})^{ABCA}$, (3) $(002)^{ACBA}$, and (4) $(220)^{ABCA}$. Red triangles indicate Bragg peaks of Cu NPs with varied orientation (see text) with (5) $(11\bar{1})$, (6) $(1\bar{1}1)$ or $(\bar{1}11)$, and (7) (200) or (020). The intensity peaks on a line along q_z arise from substrate crystal truncation rods. The H−L maps of the O-bZnO are shown in Figure S3, and extracted data are tabulated in Table S2 for both samples. Unspecified ring-like features are due to the polycrystalline Be dome of the experimental chamber.

pressure X-ray photoelectron spectroscopy (XPS), scanning tunneling microscopy (STM), and scanning electron microscopy (SEM). The experiments were performed to follow a cycle of native oxidation, reduction, interaction with CO_2, and subsequent rereduction, which is discussed for Cu/bZnO samples in the first part and for Cu/vZnO in the second part of this article.

METHODS

The sample preparation was performed at the DESY Nanolab[35] at the Centre for X-ray and Nano Science, for which an ultrahigh vacuum (UHV) system with a base pressure better than 3×10^{-11} mbar was utilized. The ZnO samples were cleaned by cycles of Ar sputtering at $p(\mathrm{Ar}) = 5 \times 10^{-6}$ mbar with $U_{acc} = 500$ V and subsequent annealing at 920 ± 50 K until LEED measurements showed sharp substrate diffraction reflexes.[25] Copper was evaporated from a molybdenum crucible onto the sample with a growth rate of 0.1 Å /min while the sample was at 570 ± 30 K, resulting in a formal Cu layer thickness of about 2 nm. These preparation conditions are identical with our previous work,[25] in which we investigated the growth and morphology of the Cu NPs on ZnO (0001), $(000\bar{1})$, and $(10\bar{1}4)$ surfaces (see Figure 1).

After native oxidation for 3−5 days at ambient air pressure and room temperature, the samples were mounted onto the heater of a computer-controlled flow cell using boron nitride paste. The temperature was calibrated under flow conditions, which has an experimental error of ±30 K. The experiments were performed at 420 and 500 K, i.e., just below and at temperatures utilized for methanol synthesis.[1] A beryllium dome acted as an X-ray window. The flow rate, pressure, and composition (Ar, H_2, and CO_2; each 99.999% purity) of the gas within the cell was regulated by mass flow and back-pressure controllers. The HE-GIXRD and XRR measurements were performed at DESY, PETRA III beamline P07 in Hamburg, Germany,[36] utilizing a beam energy of 73.4 keV. The diffraction experiments were performed with a PerkinElmer XRD 1621 flat-panel detector, whereas an FMB Oxford Ltd. CyberStar NaI detector was utilized for the XRR investigations. The 2D diffraction images were transformed from detector coordinates into reciprocal space and were evaluated with the GIDVis software.[37] For clarity, Bragg peaks are always indexed in bulk coordinates while the conversion into surface coordinates is shown in Table S1, with peak positions and error bars listed in Tables S2−S4. The ZnO substrate crystal truncation rods (CTRs) were extracted from the data sets using home-written scripts in Wavemetrics Igor Pro,[38] to which a model is fitted utilizing the ANAROD[39,40] package. The model allows surface relaxation in the out-of-plane direction and assumes a Poisson distribution for the interface roughness. The typical error in variance of ±0.05 translates to an error bar of ±0.02−0.03 layers (Figures S1 and S2).[41] The XRR data model was fitted with Fewlay,[42,43] adjusting the layer thickness, electron density, roughness, and absorption.

The HE-GIXRD and XRR experiments are supported by XPS and SEM investigations of similarly prepared Cu/ZnO samples. XPS data under UHV conditions were obtained at the Paul Scherrer Institute in Switzerland at the PEARL beamline of the Swiss Light Source at normal emission of electrons with an X-ray energy of $h\nu$ = 1070 eV,[44] whereas XPS data at 200 mbar (H_2, CO_2) were obtained at DESY, PETRA III beamline P22 in Hamburg, Germany,[45] utilizing the POLARIS endstation[46] with an X-ray incidence angle of 0.3° at $h\nu$ = 4600 eV and an effective probe depth of 1.8 nm into the sample. The SEM images were obtained at the DESY Nanolab[35] using an field emitter instrument to reveal the morphological changes after the oxidation−reduction processes.

RESULTS AND DISCUSSION

Cu/Zn-BZnO and Cu/O-BZnO Systems. HE-GIXRD measurements were performed for Cu/Zn-bZnO and Cu/O-bZnO after storage in air for 4 or 5 days respectively, to investigate the crystal structure of the particles after native oxidation. First, the samples were studied during heating to 420 K at 1 bar Ar in order to desorb water and other volatile contaminants from the surface. The HE-GIXRD results displayed in Figures 2 and S3 reveal that the Cu NPs on Zn-bZnO and O-bZnO were fully oxidized to Cu_2O during the storage period. They maintained their crystallographic orientation with respect to the underlying substrate as initiated upon the growth of the metallic Cu particles under UHV conditions.[25,47] The (111) planes were aligned parallel to the basal ZnO surfaces, and Cu_2O NPs with both ABCA and ACBA stacking are observed. As both crystalline structures were of face-centered cubic symmetry with bulk lattice constants of 3.615 Å for Cu[48] and 4.267 Å for Cu_2O,[49] the integration of oxygen into the metallic Cu NPs caused the lattice to "swell" without distortion from cubic symmetry. This

https://doi.org/10.1021/acsanm.3c01306
ACS Appl. Nano Mater. 2023, 6, 8004−8016

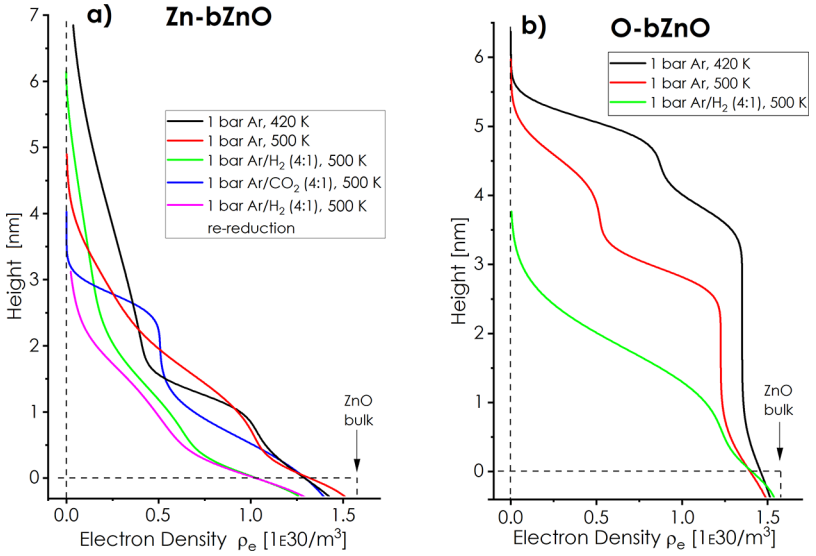

Figure 3. Electron density profiles of the NP covered (a) Zn-bZnO and (b) O-bZnO surfaces at 1 bar under the respective gas atmosphere and temperature. The profiles were calculated according to the XRR data and fits in Figure S4a,b for which structural parameters are summarized in Tables S5 and S6.

effect was reported in the literature of other systems, e.g., the $p(7 \times 7)$ structure of $Ag_2O(111)$ formation on Ag(111).[50] The Cu_2O NPs have an average diameter of $D = 6.9 \pm 0.4$ nm and a height of $H = 3.3 \pm 0.1$ nm for Cu_2O/Zn-bZnO as well as $D = 4.4 \pm 0.2$ nm and $H = 2.9 \pm 0.1$ nm for Cu_2O/O-bZnO derived from the in-plane and out-of-plane widths $\Delta q_{xy/z}$ of the respective (002) Bragg peaks (Table S2). The ring-like elongation around the Bragg peaks in Figure 2 indicates NPs mosaicities $\Delta\omega$ of 5°−9° (Table S4).

The fitting of the ZnO crystal truncation rod[51] model, according to the data measured by HE-GIXRD, reveals a root-mean-square (RMS) roughness averaged over the illuminated surface of 0.99 layers for the Zn-bZnO surface and 1.14 layers for the O-bZnO surface (Figures S1a and S2b), where one layer is half a ZnO unit cell in height representing the step height of basal ZnO surfaces.[52]

Fitting of the XRR data of the basal ZnO samples (Figure S4a,b) resulted in the electron density (ρ_e) profiles depicted in Figure 3a,b, in which a bimodal height distribution can be observed for both samples. The Zn-bZnO sample features smaller NPs with a height of 1.3 nm and larger NPs whose heights are more distributed up to 7 nm, similar to the STM images of Cu/Zn-bZnO after growth in UHV depicted in Figure 1a in which large flat NPs with individual heights up to 8 nm are surrounded by small grains of about 1 nm in height. The Cu_2O NPs on O-bZnO show a narrower distribution with heights of 3.8 and 5.1 nm, similar to Figure 1d. The integrated ρ_e profile area is a measure of the amount of material on the surface, which indicates that more than twice the amount of Cu_2O is present on O-bZnO compared to Zn-bZnO. We suspect that the formation of a few high and voluminous NPs, for which XRR is not sensitive, is accountable for the observed difference although experimental errors like an off-center evaporation geometry during the initial growth cannot completely be ruled out. The ratio of ρ_e/ρ_e^{bulk} at $H = 0.5$ nm indicates a surface coverage of 63% on Zn-bZnO and 81% on O-bZnO, which leaves the remaining area on the ZnO substrate bare for interactions with the gas phase molecules.

Before investigating the influence of reactive gas feeds, the temperature of the samples was raised from 420 to 500 K at 1 bar Ar to obtain information on the sole influence of a realistic temperature needed for methanol synthesis and CO_2 hydrogenation reactions on the samples under investigation. The HE-GIXRD data (Figures 2b and S3b, Table S2) reveal that the Cu_2O NPs on Zn-bZnO become 18% larger in average height and diameter, whereas an average increase of 56% in diameter and 16% in height for Cu_2O/O-bZnO was observed. We account NP sintering to be the predominant growth mechanism at 500 K. Because of the higher surface coverage, the NPs on O-bZnO are more closely packed on a two-dimensional plane. This enhances the general probability of sintering and increases the NPs' average diameter rather their height. Further evidence can be drawn from the decrease in surface coverage from 81% to 74% as observed in the ρ_e profiles of O-bZnO, whereas it stays constant for Zn-bZnO (Figure 3).

Contrary to the increase in NP size observed in HE-GIXRD experiments, the integrated profile area of the electron density decreases by 15% for Cu_2O/Zn-bZnO and 29% for Cu_2O/O-bZnO. We doubt that diffusion of material into the ZnO bulk, as reported for Cu/Zn-bZnO at 500 K under UHV,[53] may lead to a decrease to this extent. This is supported by the ZnO crystal truncation rod model (CTRs, Figures S1 and S2) of the HE-GIXRD data, in which negligible surface relaxation in the out-of-plane direction with layer displacements below 2% and slightly changing RMS roughnesses (from 0.99 to 0.97 layers for Zn-bZnO and from 1.14 to 1.11 layers for O-bZnO) was obtained, which points toward atomic-scale stability of the support. We suspect the formation of significantly larger particles during the sintering process to be the reason for the observed decrease in the electron density profile area, as those formations gather large amounts of material but are difficult to detect by XRR.

In the next step, surface investigations were performed under reducing conditions of 1 bar Ar/H_2 (4:1) at a flow rate of 100 mL/min at 500 K. The HE-GIXRD H−L maps in Figures 2c and S3c show that the Cu_2O was reduced to metallic Cu. The (111) orientation as well as the epitaxy of the NPs was mostly maintained during the reduction; however, Debye−Scherrer rings become visible, which show the loss of the ordered

https://doi.org/10.1021/acsanm.3c01306
ACS Appl. Nano Mater. 2023, 6, 8004−8016

interface relationship of a fraction of the NPs to the ZnO support. The NPs that remain (111) oriented change in average size from $D = 8.2 \pm 0.5$ nm and $H = 3.9 \pm 0.1$ nm to $D = 6.1 \pm 0.3$ nm and $H = 3.1 \pm 0.1$ nm for Zn-bZnO and from $D = 6.9 \pm 0.4$ nm and $H = 3.3 \pm 0.1$ nm to $D = 7.4 \pm 0.6$ nm and $H = 4.1 \pm 0.2$ nm for O-bZnO. Thus, the NP size decreases for Zn-bZnO due to the reduction from the more voluminous Cu_2O unit cell to Cu ($\Delta V_{Zn-bZnO} = -56.4\%$ assuming $V = \pi(D/2)^2H$ compared to theoretical $V_{th} = -40.3\%$); however, the NP size on O-bZnO increases ($\Delta V_{O-bZnO} = +39.9\%$), which points toward an enhanced mass transport of Cu on the reduced surface. We consider the O-terminated ZnO surface to be more vulnerable toward reduction by H_2 in comparison to Zn-bZnO, which is supported by HCl etching experiments,[54] and speculate that its partial reduction is the underlying reason for the enhanced sintering of Cu NPs. Further evidence can be drawn from the CTRs, which show only a slight increase in RMS roughness from 0.97 to 1.00 layers for Zn-bZnO while it was more pronounced for O-bZnO, increasing from 1.11 to 1.20 layers. We conclude that the O-bZnO surface in our experiments becomes partially reduced under the influence of H_2 at 500 K, resulting in the formation of Zn adatoms and O vacancies that lead to observed mass transport of the supported NPs. Zn migration from ZnO onto the surface of the Cu NPs is suspected to be the underlying reason for the strong metal–support interaction that enhances the performance of the catalyst, while it is debated if these decorations are present in the form of metallic Zn,[9] partially positively charged $Zn^{\delta+}$ located at Cu steps/defects,[11] or ZnO of wurtzite[14,19] or graphitic-like[55] structure during the catalytic reaction.

In the following, we therefore address the Cu NP lattice constants after H_2 reduction as an indicator for CuZn alloy formation according to Vegard's law.[56] The generation of CuZn bulk alloy was reported under severe reduction conditions[57] and is regarded as an irreversible and unfavored state for efficient methanol catalysts.[10] The Cu lattice constants were derived in different crystallographic directions as deformation and elastic strain can affect the unit cell. Cu NPs grown under UHV show (111) orientation on basal ZnO due to the optimization of surface energies as well as due to the coincidence lattice between the two crystal systems.[25,47] Our HE-GIXRD experiments reveal that the unit cell of the Cu NPs is compressed along the out-of-plane [111] direction and extended in the perpendicular in-plane directions for both samples. The Cu/Zn-bZnO system shows, with $a_{oop}^{Cu} = 3.617 \pm 0.011$ Å and $a_{ip}^{Cu} = 3.627 \pm 0.006$ Å, a similar strain compared to the Cu/O-bZnO system, with $a_{oop}^{Cu} = 3.618 \pm 0.007$ Å and $a_{ip}^{Cu} = 3.626 \pm 0.007$ Å. In comparison, bulk Cu has a lattice parameter of 3.615 Å[58] at room temperature and expands to 3.626 Å[59] at 500 K. The commensurable interface between Cu (111) and ZnO (0001) planes with $5a_0^{Cu}/\sqrt{2} \approx 4a_0^{ZnO}$ has, according to bulk values, a misfit of −1.72% at 500 K.[59,60] The experimentally observed Cu lattice parameter after the oxidation–reduction cycle is in good agreement with the literature values with interface misfits of −1.69% for Cu/Zn-bZnO and −1.72% for Cu/O-bZnO. Despite the distortion of the unit cell, the observed lattice parameters are equal to or lower than literature values for bulk Cu. Estimating the effect of Vegard's law at 500 K, the formation of a CuZn bulk alloy with 5 wt % Zn would increase the lattice parameter to about 3.638 Å.[61] We can therefore exclude bulk alloying, i.e., the uptake of Zn from the ZnO lattice, under these reducing conditions. The applied experimental conditions of 500 K at 1 bar represent an intermediate case in comparison to the systematic study of Beck et al.,[62] in which the onset of CuZn formation was observed between 470 and 570 K at 1 bar or between 1 and 10 bar at 470 K.

The XRR investigations show that the ρ_e profile area continued decreasing under reducing conditions, i.e., by 36% for the NPs on Zn-bZnO and 48% for the NPs on O-bZnO, of which only 12% can be accounted to the loss of lattice O during the reduction to metallic Cu. This, together with the appearance of Debye–Scherrer rings, points toward the agglomeration of individual NPs into larger formations of randomly oriented grains. However, additional intensity maxima located on the circumference of the Debye–Scherrer rings can be identified for Cu/Zn-bZnO (red triangles in Figure 2c) while no such signals are discernible in the case of Cu/O-bZnO. These peaks correspond to features with a smaller diameter $D = 3.6 \pm 0.4$ nm but a greater height $H = 4.9 \pm 1.3$ nm, with a difference in lattice parameter of 0.2% compared to the (111) oriented Cu NPs (Table S2). Those features either may originate from internal NP twinning of $(11\bar{1})$ planes or are due to the formation of Cu NPs with altered orientation during mass transport.

Next, we will discuss the interactions of the reduced model catalysts with CO_2, as it is used in synthesis gas feeds during methanol synthesis and reverse water-gas shift reactions, where it acts as the carbon source.[18,63] It effectively acts as an oxidizing and reducing agent simultaneously, as the reaction to more complex products requires its dissociation into a CO and an O species. Under 100 mL/min flow of Ar/CO_2 (4:1) at 1 bar, the HE-GIXRD investigations (Figure 2d) revealed surprisingly a complete absence of any Bragg peaks and Debye–Scherrer rings related to Cu or Cu_2O nor to Zn or CuZn alloy for the Cu/Zn-bZnO sample (no data were recorded for Cu/O-bZnO). This suggests that the Cu NPs transitioned into an amorphous state during the CO_2 treatment. To explore the chemical state of Cu under CO_2 conditions, ambient pressure XPS investigations were performed on a similarly prepared Cu/O-bZnO sample after about 1 h of native oxidation at room temperature and ambient air pressure (Figure 4). Under 200 mbar of H_2 at 500 K, the NPs consist of either Cu or Cu_2O, which both give rise to peaks at 933.0 and 952.8 eV in the Cu 2p spectrum (no Cu LMM Auger peaks were recorded). Under 200 mbar of CO_2 at 500 K, major contributions of Cu^{2+} species are revealed, which we interpret as clear evidence for the formation of CuO (Figure 4); however, the Cu 2p peaks still show shoulders that originate from minor contributions of Cu or Cu_2O. We expect no differences for the change in oxidation state of the Cu species under CO_2 regarding the difference in termination of the Zn-bZnO or O-bZnO substrate.

During the oxidation by the exposure to CO_2, the ρ_e profile area (Figure 3) increased by 37%, of which 27% can be accounted to the uptake of oxygen into the NPs. Presumably, the change in structure from fcc-type Cu to amorphous CuO redisperses material from larger agglomerates to the surface, which becomes observable by XRR again. A similar effect was noted after 9 months of native oxidation for Cu/vZnO where elongated NPs separate into smaller fragments (Figure 6). The surface coverage increased from 39% to 62%, which supports this argument. No indication for the formation of wurtzite or rock-salt ZnO by oxidation of suspected Zn adatoms was

https://doi.org/10.1021/acsanm.3c01306
ACS Appl. Nano Mater. 2023, 6, 8004–8016

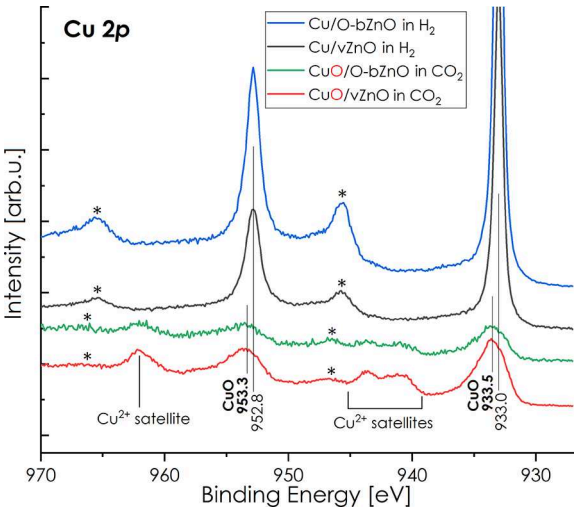

Figure 4. Ambient pressure XPS Cu 2p spectra of Cu/O-bZnO and Cu/vZnO at 500 K in 200 mbar of H_2 or CO_2, respectively. The maxima at 933.5 and 953.3 eV relate to Cu $2p_{3/2}$ and $2p_{1/2}$ of CuO, whereas the shoulders at 933.0 and 952.8 eV are the respective features for Cu or Cu_2O. Asterisks point out features that are due to inelastic scattering with the gas phase.[64] Spectra were translated vertically.

found, while graphitic-like ZnO presumably has an insufficient long-range order to be observable in the diffraction data.[55] The RMS roughness of the Zn-bZnO surface, as derived by the ZnO CTR data (Figure S1c,d), decreased slightly from 1.00 under Ar/H_2 to 0.92 layers under Ar/CO_2 conditions, which shows the stability of the Zn-terminated support under oxidizing conditions. We propose the following scheme for the oxidation of the Cu NPs under 1 bar of Ar/CO_2 at 500 K. The CO_2 dissociates into a CO and an O species at the Cu surface steps.[20] As the gas feed was deficient in H_2 or other reducing agents, the O species oxidizes the NPs surface to CuO. The crystal lattice changes from fcc to monoclinic, which ruptures the NPs surface allowing the generation of CuO further inside. The CO species bind to the Cu surfaces after the rupture and increase the mobility of the surface atoms to form round smaller round fragments.[65,66] Additionally, they sterically hinder the introduction of short-range order during oxidation as they are generated in a 1:1 ratio for each Cu−O pair, leading to an amorphous phase. Partial reoxidation of the CO species, especially by low-coordinated surface O of the amorphous CuO phase, can be expected within a steady-state equilibrium.

Reversibility and degradation during oxidation−reduction cycles are important issues for the long-term performance of a catalyst; thus, we re-reduced the CuO/Zn-bZnO sample in Ar/H_2 (4:1) at 500 K to identify the structural changes compared to the previous reduction cycle. The HE-GIXRD maps (Figure

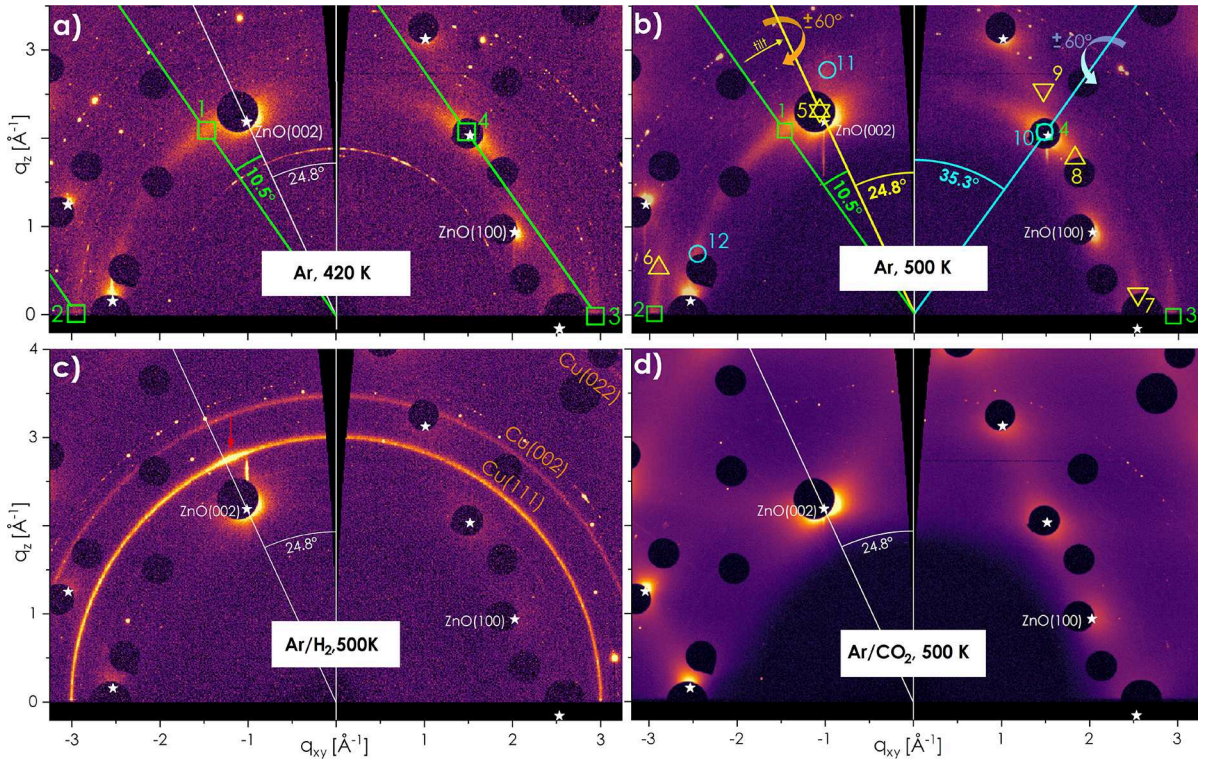

Figure 5. H−$L^{(10\bar{1}4)}$ maps of vZnO$(10\bar{1}4)$ at (a) 420 K in Ar, (b) 500 K in Ar, (c) Ar/H_2 at 500 K, and (d) Ar/CO_2 at 500 K with gas feeds of 1 bar, 100 mL/min, and (4:1) mixture ratio, respectively. The images were obtained by transformation from detector coordinates to reciprocal space[37] and summation of frames from an azimuthal rotation of $\omega = 0.5 \pm 0.1°$ plus $3.5 \pm 0.1°$ from the NPs (111) peak centered at $\omega = 0°$. Green squares: (1) (111), (2) $(002)^{ABCA}$, (3) $(00\bar{2})^{ABCA}$, and (4) theoretical $(11\bar{1})^{ABCA}$ position. Yellow triangles: (5) theoretical (111) position, (6) $(002)^{ABCA}$, (7) $(\bar{1}\,\bar{1}1)^{ACBA}$, (8) theoretical $(11\bar{1})^{ABCA}$ position, and (9) $(002)^{ACBA}$. Cyan circles: (10) theoretical $(11\bar{1})$ position, (11) {200}, and (12) $\{1\bar{1}1\}$. Underlying Debye−Scherrer rings of Cu in (c) are visible for all azimuthal angles while the orientation of Cu [111] parallel to [002] of the vZnO substrate is slightly preferred (red arrow and Figure S6). Unnamed ring-like features are due to the polycrystalline Be dome of the experimental chamber and Ta contamination from the clips used for mounting the sample during preparation under UHV (Figure S7).[25,67]

https://doi.org/10.1021/acsanm.3c01306
ACS Appl. Nano Mater. 2023, 6, 8004−8016

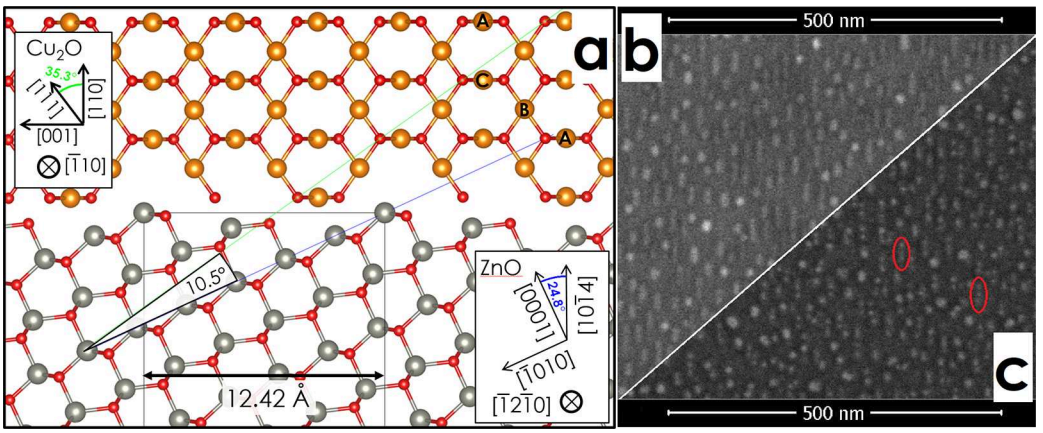

Figure 6. (a) Model of ABCA stacked Cu_2O on vZnO with an angle of 10.5° between the Cu_2O (111) and ZnO (0001) planes, which corresponds to the green labeled features in Figure 5a,b. A model of ACBA stacked Cu_2O/vZnO, which was not experimentally observed, is shown in Figure S8d. Right: SEM images of Cu/vZnO after (b) 3 days and (c) 9 months of native oxidation.

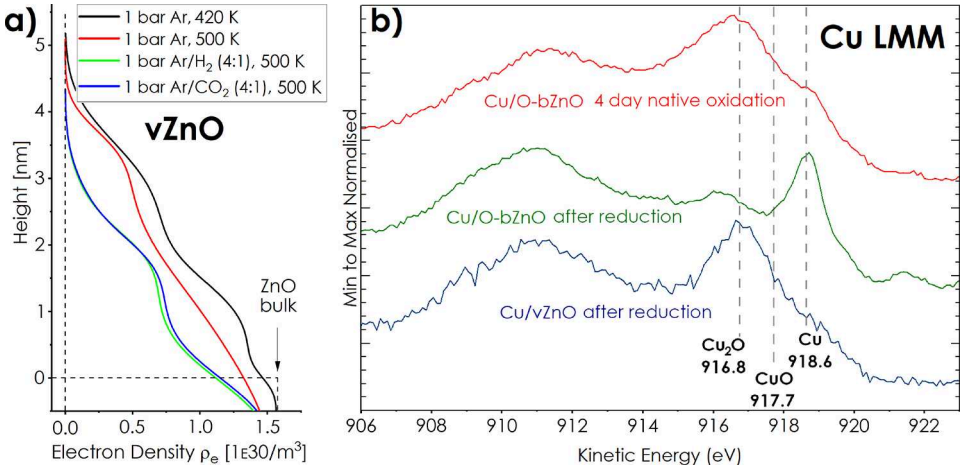

Figure 7. (a) Electron density profiles of the NP-covered vZnO surface at 1 bar under the respective gas atmosphere and temperature. (b) XPS measurements of Cu Auger features of Cu/O-bZnO and Cu/vZnO. Respective Cu 2p core levels are displayed in Figure S11.

2e) reveal Debye−Scherrer rings of metallic Cu with an average domain size of 6.05 nm, which signifies the loss of the interfacial relationship between Cu and ZnO. The RMS roughness (Figure S2a) of the ZnO support, as well as its surface coverage with Cu, restored to the values of the previous cycle, namely 1.01 layers and 40%, respectively, yet the integrated electron density decreased by 29% (48% compared to Ar/CO_2 conditions; Figure 3). This, again, signifies agglomeration of the NPs which can be confirmed by SEM images of all investigated samples after the oxidation−reduction cycles (Figure S5).

Cu/vZnO System. HE-GIXRD investigations of the Cu NPs on the vicinal ZnO(10$\bar{1}$4) sample were performed after 3 days of storage in air to investigate the crystal structure of the particles after native oxidation. The sample was heated to 420 K at 1 bar Ar in order to desorb water and other volatile contaminants from the surface, while HE-GIXRD data were collected. The initially metallic Cu NPs completely oxidized to Cu_2O in parallel to the observations obtained for NPs on basal ZnO (Figure 5a). They are on average $H = 2.3 \pm 0.1$ nm in height and $W = 3.0$ to 7.4 nm in width, inferred from the radial widths of the (111) and (002) Bragg peaks, respectively.[a]

The Cu_2O NPs maintain two key features that have been previously reported[25] for the metallic NPs. First, the presence of ABCA stacked NPs can be identified by the Cu_2O (002) and (00$\bar{2}$) Bragg peaks, whereas no signal can be observed for ACBA stacking. This originates from the direct interaction of each (111) plane of the NPs with the substrate before oxidation, as they are not parallel to the vZnO surface.[25] As this favored stacking is maintained during the native oxidation of the NPs to Cu_2O, we conclude that no significant interparticular mass transport took place during oxidation in air. Second, the Cu_2O(111) Bragg peak is located on the high symmetry H−$L^{(10\bar{1}4)}$ plane of the vZnO(10$\bar{1}$4) substrate. For metallic Cu/vZnO, the Cu(111) Bragg peak is at an angle of 25.6° to the vZnO surface normal, whereas the Cu_2O(111) Bragg peak shows an angle of 35.3°, effectively aligning the Cu_2O(110) plane parallel to the vZnO surface.

This angular change indicates that the NPs "rotate" around an axis parallel to the ZnO surface rows, i.e., the ZnO (1210) plane during oxidation, in addition to the swell of the fcc lattice. Figure 6a shows a real space model of the crystallographic orientation of Cu_2O with ABCA stacking of (111) planes on the vZnO surface. Similar to the commensurability relationship of Cu/Zn-bZnO, Cu/O-bZnO,[47] or Cu/vZnO,[25] a coincidence lattice can be identified, where $3a_0^{Cu_2O}$ matches the step distance of the vicinal ZnO surface with a misfit of +3.06%. Furthermore, (1$\bar{1}$1) and ($\bar{1}\,\bar{1}$1) become in-plane

https://doi.org/10.1021/acsanm.3c01306
ACS Appl. Nano Mater. 2023, 6, 8004−8016

peaks with q_z = 0, which may point toward another commensurability relationship parallel to the surface rows. The commensurable matching provides a plausible energetic minimum for the observed reorientation of the NPs. We speculate that the reorientation is enabled during the nonuniform swelling during the oxidation progresses, rather than being due to a thermally driven rotation. Fitting of the XRR data model (Figure S4c) resulted in the ρ_e profiles depicted in Figure 7a, for which Table S7 summarizes the structural parameters. In analogy to the basal samples, the height distribution of Cu_2O NPs on vicinal ZnO is bimodal with 1.44 and 3.54 nm, which is in agreement with the averaged value of 2.3 nm as obtained from HE-GIXRD. The surface coverage is with 82% equal to the observed value for Cu_2O NPs on O-bZnO.

To gain insight into the long-term progression of the native oxidation process, its advancement was followed by obtaining SEM images of an equally prepared Cu/vZnO sample after 3 days and 9 months of native oxidation at ambient pressure and room temperature. After 3 days (Figure 6b), the shape of the Cu_2O NPs stayed in good agreement with the morphology of Cu NPs investigated by STM after initial growth under UHV conditions.[25] After 9 months of storage in air—a period for which CuO formation was reported for bulk Cu[32]—the SEM images (Figure 6c) reveal lines of round NPs with a diameter similar to the width of the previously elongated Cu_2O NPs. We presume that the transition from the fcc-type crystal lattice of Cu_2O to the monoclinic lattice structure of CuO leads to the fragmentation of the elongated NPs into smaller individual particles.[b] The transition to CuO supposedly resembles a point of no return in diminishing the large-sized, densely stepped facets, which were observed for Cu/vZnO after growth under UHV conditions.[25] However, for the transition from Cu to Cu_2O no indication of a morphology change that would lead to a similar conclusion has been observed at 420 K under 1 bar of Ar.

In the following, we discuss the stability of the Cu_2O NPs on vZnO at 500 K under 1 bar of Ar, which is a realistic temperature needed for methanol synthesis and CO_2 hydrogenation reactions. The HE-GIXRD data in Figure 5b reveal that the previously described NP orientation, with $Cu_2O(110)$ planes being parallel to the surface substrate, is still observed as the most prevalent species. Their average size increased by 27% in height to H = 2.9 ± 0.2 nm and in width by 30% to 3.9−9.6 nm (Table S2), similar to the Cu NPs on basal ZnO during this step. Additionally, two new orientations of Cu_2O NPs can be observed, which are detailed in Section S4 of the Supporting Informationand will be briefly addressed in the following. First, features of Cu_2O NPs arise that indicate an alignment of their (111) plane parallel to the ZnO (0001) planes (yellow triangles 5−9 in Figure 5b) for which equal ABCA and ACBA stacking can be discerned. Second, faint features (cyan circles 10−12 in Figure 5b) appeared, which originate either from the twinning of the $(11\bar{1})$ planes or from effectively "rotating" the NPs around their $[11\bar{1}]$ axis by ±60°. As ACBA stacked Cu_2O NPs of the original orientation type were not observed, we conclude that the new features arise due to the formation of new NPs during mass transport rather than the introduction of twinning defects. A similar mechanism was observed for the NPs on Zn-bZnO, but notably only after the reduction step in H_2.

The XRR investigations (Figure S4c) result in electron density profiles (Figure 7a) with summarized fitting parameters tabulated in Table S7. The surface coverage at H = 0.5 nm decreases from 82% at 420 K to 67% at 500 K along with a decrease of 17% of the integrated electron density. This seeming loss of material can be explained by agglomeration to voluminous particles during mass transport, for which XRR is not sensitive. Smaller NPs have higher mobility on the surface due to a lower interface area to the support, which leads to a decrease in the ZnO surface coverage upon sintering/agglomeration. The surface roughness of the substrate increased from 2.0 Å at 420 K to 8.0 Å at 500 K, which differs from the observation of basal ZnO where consistent (O termination) or decreasing (Zn termination) values have been obtained after increasing the temperature. This roughening of the vicinal surface explains the mobilization of small NPs at an earlier step in the experimental sequence compared to Zn-bZnO, as it indicates a detachment within the Cu−ZnO interface.

In the next step, we discuss the reduction of the Cu_2O NPs. XPS investigations of a similarly prepared and natively oxidized Cu_2O/vZnO sample were performed to obtain chemical information during the reduction process. After a 2.5 h long mild reduction at 3×10^{-7} mbar of H_2 and 500 K, the spectra revealed that the particles remained oxidized to Cu_2O with low contributions of CuO present on the surface (Figures 7b and S11). In comparison, a Cu_2O/O-bZnO sample was successfully reduced to mostly metallic Cu after 1 h under the same reduction conditions. This difference between the samples points toward higher kinetic barriers for the reduction of the NPs on vZnO. Bao et al.[68] reported that (111) facets of Cu_2O are more easily reduced due to the presence of lower-coordinated Cu surface atoms in comparison to their (100) facets. We suspect that the higher kinetic barriers for reduction are due to a lower fraction of $Cu_2O(111)$ facets compared to the NPs on basal ZnO, although an inhibition by a thin layer of CuO cannot be excluded.

Continuing the experimental sequence of the HE-GIXRD investigations, the gas feed of the Cu_2O/vZnO system at 500 K was changed from Ar to Ar/H_2 (4:1). A pressure of 1 bar with a flow rate of 100 mL/min was found to be sufficient for the reduction of the NPs. Figure 5c shows Cu Debye−Scherrer rings with a (111) intensity maximum at a 23.38° angle from the substrates' surface normal in the $H-L^{(10\bar{1}4)}$ plane. A large fraction of the NPs lost their interfacial order to the ZnO support and disoriented during the reduction, while others aligned their Cu (111) planes parallel to the (0001) planes of the vZnO in analogue to the initial Cu NPs prepared under UHV conditions.[25] These NPs do not maintain the preference of ABCA over ACBA stacking order, as Cu Bragg peaks of both stacking orders are visible near the K−L plane of the vZnO system with the expected intensity ratios of equally abundant ACBA and ABCA stacked NPs (Figure S6). We conclude that the aligned NPs were newly formed during mass transport under the reduction conditions. Their average size amounts to 8.3 ± 0.7 nm, while the randomly oriented Cu NPs show average sizes between 18.5 and 28.6 nm (Table S2).

Re-examining the data of Cu/vZnO measured at room temperature under 1 bar of Ar before the oxidation−reduction cycle[25] reveals an experimentally obtained coincidence lattice misfit of −1.25% between Cu (111) and ZnO (0001) planes. After native oxidation and reduction, the misfit amounts to −1.69% as measured at 500 K under 1 bar of Ar/H_2 (4:1), which is similar to the values of −1.69% for Cu/Zn-bZnO and

https://doi.org/10.1021/acsanm.3c01306
ACS Appl. Nano Mater. 2023, 6, 8004−8016

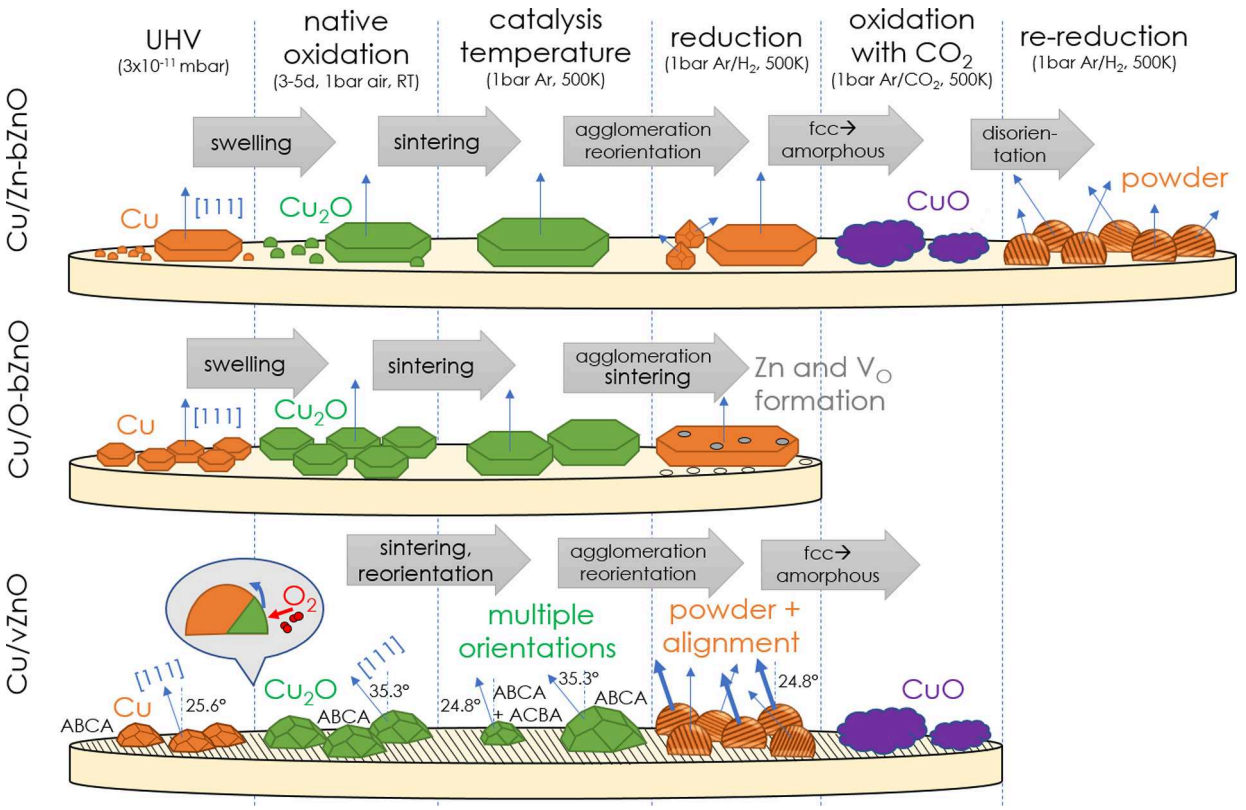

Figure 8. Scheme of the evolution of Cu NPs on Zn-bZnO, O-bZnO, and vZnO during the oxidation−reduction cycle.

−1.72% for Cu/O-bZnO after the oxidation−reduction cycle. As the misfit of the Cu−ZnO coincidence lattice accumulates over several unit cells, an alignment between Cu (111) and ZnO(0001) planes becomes less favorable, which explains the observation of the smaller sizes of aligned NPs compared to the randomly oriented NPs.

The electron density profile in Figure 7a shows a decrease in ZnO surface coverage from 67% to 28% upon reduction, along with a decrease in integrated electron density decreased by 37%. The NPs appear to become more uniform in height with about H = 2.3 nm, which is in contrast to the average NPs sizes of 8.3 nm (aligned) and 18.5−28.6 nm (ring) determined by HE-GIXRD. We account an ongoing agglomeration into larger NPs assemblies, for which XRR is not sensitive, to be the reason for the measured decrease in electron density and NP height.

Finally, we will discuss the HE-GIXRD (Figure 5d) and XPS (Figure 4) observations garnered for the reduced Cu/vZnO sample under the influence of a CO_2-rich gas feed at 500 K at 1 bar or 200 mbar, respectively. In analogy to the NPs on basal ZnO, the investigations revealed the absence of any Bragg peaks and Debye−Scherrer rings related to Cu, Cu_2O, Zn, or CuZn alloy as well as the prevalence of Cu^{2+} with low contributions of Cu or Cu_2O in the Cu 2p spectra. We conclude that an amorphous CuO phase was generated under these oxidizing/reducing conditions, following a similar oxidation mechanism as discussed for basal ZnO. The ρ_e profiles (Figure 7a) under reducing H_2 and oxidizing CO_2 conditions are almost identical. Such an observation is in contrast to the HE-GIXRD and XPS data as well as to the observations on basal ZnO samples, which signifies that heavily agglomerated NPs are not detected by XRR investigations. The SEM images depicted in Figure S5 are obtained after the experimental oxidation−reduction sequence and confirm the cauliflower-like agglomerate formation for all investigated samples.

SUMMARY AND CONCLUSION

The experimental observations of Cu NPs on basal and vicinal ZnO supports during the oxidation−reduction cycle are summarized in Figure 8. The native oxidation of Cu NPs resulted in fully oxidized Cu_2O NPs on all investigated supports. Cu_2O NPs on bZnO maintained their orientation to the substrate while the nanosized crystals tilted coherently on vZnO, resulting in a commensurable interface relationship between Cu_2O (001) and the vZnO surface steps. The integration of oxygen into the Cu NPs caused the crystal lattice to swell without major distortion from an fcc structure. At 500 K, mass transport in the form of Cu_2O NP sintering was observed. For Cu_2O/vZnO, this leads to diffraction signals originating in NPs of altered orientation. The reduction under Ar/H_2 at 500 K significantly increased the NP mosaicity, observable as Debye−Scherrer rings in the diffraction data. However, the initial Cu/vZnO interface relation as observed after growth in UHV was partially reestablished, which potentially leads to similar large-sized facets that present a high abundance of low-coordinated Cu surface atoms. XPS investigations indicated a higher kinetic energy barrier for the reduction of Cu_2O/vZnO in H_2. The reduction of Cu_2O to Cu on O-bZnO was accompanied by enhanced Cu mass transport, which indicates a higher vulnerability of the O-terminated basal ZnO surface against H_2 and points toward mild Zn adatom and O vacancy formation. The presence of such defects can neither be confirmed nor be excluded for Zn-bZnO or vZnO, yet no CuZn bulk alloying of NPs was observed. The Cu NPs oxidized in Ar/CO_2 at 500 K to amorphous CuO. We

https://doi.org/10.1021/acsanm.3c01306
ACS Appl. Nano Mater. 2023, 6, 8004−8016

propose that as CO_2 dissociates into a CO and an O species, an induced change in lattice structure from fcc (Cu) to monoclinic (CuO) initiated the rupture of the NPs during the uptake of oxygen. While this allowed further oxidation within the NP itself, the CO species sterically hinders the generation of long-range order, resulting in an amorphous CuO phase. Rereduction of CuO/Zn-bZnO by H_2 resulted in Cu powder that showed no preferential alignment to the underlying support.

We come to the following conclusions: Cu_2O NPs already sinter and agglomerate under an inert gas atmosphere at 500 K prior to their reduction. Under 1 bar of H_2 at 500 K, the NPs reduce to metallic Cu accompanied by mild sintering. CuZn bulk alloying can be excluded under these conditions. The facet-specific orientation of Cu NPs remains more defined for basal ZnO surfaces in comparison to vicinal ZnO. Nevertheless, the unique Cu/vZnO interfacial relationship can partially be restored during reduction. This proof-of-concept implies that an elevated abundance of low-coordinated Cu surface sites can be maintained, which are suspected to be a prerequisite for an efficient turnover of CO_2 to methanol.[11,20,21,26,69] CO_2-rich gas conditions with a deficiency of reducing agents lead to a complete material redistribution as the NPs oxidize to CuO. The epitaxy of Cu or Cu_2O NPs on vZnO is disturbed during this process, which implies that CuO formation needs to be avoided to maintain the orientation synergies for any potential application. Finally, the CTR data analysis shows that the basal ZnO surfaces stay atomically smooth under all conditions investigated, ruling out enhanced Cu/ZnO intermixing.

The approach of utilizing model catalysts enabled the use of surface science techniques, which are otherwise inaccessible for powder samples. By this, key details of the complex structural interplay between basal and stepped ZnO and Cu surfaces have been revealed. In upcoming work, we strive to extend the investigations from the UHV and ambient pressure regime toward operando conditions, utilizing $H_2/CO/CO_2$ gas feeds at 50 bar and 500 K.[70]

■ ASSOCIATED CONTENT

Supporting Information

The Supporting Information is available free of charge at https://pubs.acs.org/doi/10.1021/acsanm.3c01306.

Section S1 showing the CTR data of Zn-bZnO and O-bZnO for the experimental oxidation and reduction conditions (Figures S1 and S2); Figure S3: HE-GIXRD H−L maps of Cu_2O and Cu NPs on O-bZnO; conversions of ZnO Bragg peaks from bulk coordinates to $(10\bar{1}4)$ surface coordinates (Table S1); summarized parameters of HE-GIXRD features (Figures S2−S4); Section S3 detailing the fitting of the XRR data in Figure S4 and summarizing the obtained parameters in Tables S5−S7; SEM images of Zn-bZnO, O-bZnO, and vZnO samples after the experimental oxidation−reduction sequence (Figure S5); HE-GIXRD map near the K−$L^{(10\bar{1}4)}$ plane of reduced Cu/vZnO (Figure S6); Ta Debye−Scherrer rings originating from screws of the experimental chamber (Figure S7); additional information on the Cu_2O/vZnO with altered orientation with a depiction of respective interface models (Figure S8); line scans over the faint features 9 and 11 of Figure 5b (Figure S9); SEM images of Cu/vZnO after 9 months of native oxidation (Figure S10); UHV-XPS Cu 2p data of Cu/O-bZnO and Cu/vZnO after native oxidation and mild reduction at 3×10^{-7} mbar of H_2 and 500 K (Figure S11) (PDF)

■ AUTHOR INFORMATION

Corresponding Author

Andreas Stierle − *Centre for X-ray and Nano Science CXNS, Deutsches Elektronen-Synchrotron DESY, 22607 Hamburg, Germany; Fachbereich Physik, Universität Hamburg, 20355 Hamburg, Germany;* orcid.org/0000-0002-0303-6282; Email: andreas.stierle@desy.de

Authors

Robert Gleißner − *Centre for X-ray and Nano Science CXNS, Deutsches Elektronen-Synchrotron DESY, 22607 Hamburg, Germany; Fachbereich Physik, Universität Hamburg, 20355 Hamburg, Germany; The Hamburg Centre for Ultrafast Imaging, 22607 Hamburg, Germany;* orcid.org/0000-0003-3850-0687

Simon Chung − *Centre for X-ray and Nano Science CXNS, Deutsches Elektronen-Synchrotron DESY, 22607 Hamburg, Germany;* orcid.org/0000-0001-8087-8793

Guilherme D. L. Semione − *Centre for X-ray and Nano Science CXNS, Deutsches Elektronen-Synchrotron DESY, 22607 Hamburg, Germany; Fachbereich Physik, Universität Hamburg, 20355 Hamburg, Germany;* orcid.org/0000-0003-2210-337X

Leon Jacobse − *Centre for X-ray and Nano Science CXNS, Deutsches Elektronen-Synchrotron DESY, 22607 Hamburg, Germany;* orcid.org/0000-0002-2825-0963

Michael Wagstaffe − *Centre for X-ray and Nano Science CXNS, Deutsches Elektronen-Synchrotron DESY, 22607 Hamburg, Germany;* orcid.org/0000-0002-2795-829X

Steffen Tober − *Centre for X-ray and Nano Science CXNS, Deutsches Elektronen-Synchrotron DESY, 22607 Hamburg, Germany; Fachbereich Physik, Universität Hamburg, 20355 Hamburg, Germany;* orcid.org/0000-0002-6563-6072

A. Joanne Neumann − *Centre for X-ray and Nano Science CXNS, Deutsches Elektronen-Synchrotron DESY, 22607 Hamburg, Germany; Fachbereich Physik, Universität Hamburg, 20355 Hamburg, Germany;* orcid.org/0000-0002-8808-5090

Gökhan Gizer − *Institute of Hydrogen Technology, Materials Technology, Helmholtz-Zentrum Hereon GmbH, 21502 Geesthacht, Germany;* orcid.org/0000-0002-1268-8610

Christopher M. Goodwin − *Department of Physics, Stockholm Universitet, 10691 Stockholm, Sweden;* orcid.org/0000-0002-0062-0643

Markus Soldemo − *Department of Physics, Stockholm Universitet, 10691 Stockholm, Sweden;* orcid.org/0000-0003-0483-0602

Mikhail Shipilin − *Department of Physics, Stockholm Universitet, 10691 Stockholm, Sweden;* orcid.org/0000-0003-1623-1578

Patrick Lömker − *Deutsches Elektronen-Synchrotron DESY, 22607 Hamburg, Germany;* orcid.org/0000-0002-5297-710X

Christoph Schlueter − *Deutsches Elektronen-Synchrotron DESY, 22607 Hamburg, Germany;* orcid.org/0000-0002-8745-3074

https://doi.org/10.1021/acsanm.3c01306
ACS Appl. Nano Mater. 2023, 6, 8004−8016

Olof Gutowski − *Deutsches Elektronen-Synchrotron DESY, 22607 Hamburg, Germany;* orcid.org/0000-0001-5514-4480
Matthias Muntwiler − *Paul-Scherrer Institute, 5232 Villigen, Switzerland;* orcid.org/0000-0002-6628-3977
Peter Amann − *Department of Physics, Stockholm Universitet, 10691 Stockholm, Sweden*
Heshmat Noei − *Centre for X-ray and Nano Science CXNS, Deutsches Elektronen-Synchrotron DESY, 22607 Hamburg, Germany;* orcid.org/0000-0003-1294-3527
Vedran Vonk − *Centre for X-ray and Nano Science CXNS, Deutsches Elektronen-Synchrotron DESY, 22607 Hamburg, Germany;* orcid.org/0000-0001-9854-1101

Complete contact information is available at: https://pubs.acs.org/10.1021/acsanm.3c01306

Notes

The authors declare no competing financial interest.

■ ACKNOWLEDGMENTS

We acknowledge DESY (Hamburg, Germany), a member of the Helmholtz Association HGF, for the provision of experimental facilities. Parts of this research were performed at PETRA III using beamlines P07 and P22. Beamtime was allocated for proposals I-20181122 and I-20180782. We acknowledge the Paul Scherrer Institut in Villigen, Switzerland, for provision of synchrotron radiation beamtime at beamline PEARL of the Swiss Light Source. The authors thank Simon Geile for the assistance in the setup of the experiments as well as Martin Etter. This work is financially supported by the Cluster of Excellence "CUI: Advanced Imaging of Matter" of the German Research Foundation (DFG, EXC 2056 - project ID 390715994) and the Helmholtz Association (HGF) through the Helmholtz-Lund International Graduate School (HELIOS, HIRS-0018). The authors declare no other sources of funding.

■ ADDITIONAL NOTES

[a]($\bar{1}\,\bar{1}\,1$) and ($1\bar{1}1$) peaks were blocked with tungsten beam stops (black circles in Figure [5]) which protect the detector from the high intensity reflections of the ZnO single crystal. [b]We want to point out that also areas on the same sample were imaged where the separation into smaller particles was less progressed (Figure S10).

■ REFERENCES

(1) Zhong, J.; Yang, X.; Wu, Z.; Liang, B.; Huang, Y.; Zhang, T. State of the art and perspectives in heterogeneous catalysis of CO_2 hydrogenation to methanol. *Chem. Soc. Rev.* **2020**, *49*, 1385−1413.
(2) Cheng, Z.; Jiang, C.; Sun, X.; Lan, G.; Wang, X.; He, L.; Li, Y.; Tang, H.; Li, Y. Insights into the Inducing Effect of Aluminum on Cu−ZnO Synergy for Methanol Steam Reforming. *Ind. Eng. Chem. Res.* **2022**, *61*, 11699−11707.
(3) Li, D.; Xu, F.; Tang, X.; Dai, S.; Pu, T.; Liu, X.; Tian, P.; Xuan, F.; Xu, Z.; Wachs, I. E.; Zhu, M. Induced activation of the commercial $Cu/ZnO/Al_2O_3$ catalyst for the steam reforming of methanol. *Nature Catalysis* **2022**, *5*, 99−108.
(4) Chen, W.-H.; Chen, C.-Y. Water gas shift reaction for hydrogen production and carbon dioxide capture: A review. *Applied Energy* **2020**, *258*, 114078.
(5) Wang, Y.; Fan, S.; Xiao, Z.; Mai, Z.; Bai, K.; Chen, J.; Chen, Y.; Liu, J. Catalytic membrane nano reactor with Cu/ZnO in situ immobilized in membrane pores for methanol dehydrogenation to formaldehyde. *J. Membr. Sci.* **2022**, *643*, 120014.
(6) Wang, N.; Quan, Y.; Zhao, J.; Li, H.; Ren, J. Highly active CuZn/SBA-15 catalyst for methanol dehydrogenation to methyl formate: Influence of ZnO promoter. *Molecular Catalysis* **2021**, *505*, 111514.
(7) Batteiger, V.; Abner, K.; Habersetze, A.; Moser, L.; Schmidt, P.; Weindorf, W.; Rakscha, T. Power-to-Liquids — A scalable and sustainable fuel supply perspective for aviation. Federal Environment Agency of Germany, 2022; https://www.umweltbundesamt.de/sites/default/files/medien/376/publikationen/background_paper_power-to-liquids_aviation_2022.pdf (accessed 2022-06-30).
(8) IRENA; Institute, M. Innovation Outlook: Renewable Methanol. International Renewable Energy Agency, Abu Dhabi, 2021; https://www.irena.org/-/media/Files/IRENA/Agency/Publication/2021/Jan/IRENA_Innovation_Renewable_Methanol_2021.pdf (accessed 2022-06-30).
(9) Nakamura, J.; Choi, Y.; Fujitani, T. On the issue of the active site and the role of ZnO in Cu/ZnO methanol synthesis catalysts. *Top. Catal.* **2003**, *22*, 277−285.
(10) Frei, E.; Gaur, A.; Lichtenberg, H.; Zwiener, L.; Scherzer, M.; Girgsdies, F.; Lunkenbein, T.; Schlögl, R. Cu−Zn alloy formation as unfavored state for efficient methanol catalysts. *ChemCatChem* **2020**, *12*, 4029−4033.
(11) Behrens, M.; Studt, F.; Kasatkin, I.; Kühl, S.; Hävecker, M.; Abild-Pedersen, F.; Zander, S.; Girgsdies, F.; Kurr, P.; Kniep, B.-L.; Tovar, M.; Fischer, R. W.; Nørskov, J. K.; Schlögl, R. The active site of methanol synthesis over $Cu/ZnO/Al_2O_3$ industrial catalysts. *Science* **2012**, *336*, 893−897.
(12) Lunkenbein, T.; Schumann, J.; Behrens, M.; Schlögl, R.; Willinger, M. G. Formation of a ZnO overlayer in industrial $Cu/ZnO/Al_2O_3$ catalysts induced by strong metal-support interactions. *Angewandte Chemie (International ed. in English)* **2015**, *54*, 4544−4548.
(13) Wu, Y. A.; McNulty, I.; Liu, C.; Lau, K. C.; Liu, Q.; Paulikas, A. P.; Sun, C.-J.; Cai, Z.; Guest, J. R.; Ren, Y.; Stamenkovic, V.; Curtiss, L. A.; Liu, Y.; Rajh, T. Facet-dependent active sites of a single Cu_2O particle photocatalyst for CO_2 reduction to methanol. *Nature Energy* **2019**, *4*, 957−968.
(14) Kattel, S.; Ramírez, P. J.; Chen, J. G.; Rodriguez, J. A.; Liu, P. Active sites for CO_2 hydrogenation to methanol on Cu/ZnO catalysts. *Science (New York, N. Y.)* **2017**, *355*, 1296−1299.
(15) Porosoff, M. D.; Yan, B.; Chen, J. G. Catalytic reduction of CO_2 by H_2 for synthesis of CO, methanol and hydrocarbons: challenges and opportunities. *Energy Environ. Sci.* **2016**, *9*, 62−73.
(16) Kattel, S.; Liu, P.; Chen, J. G. Tuning selectivity of CO_2 hydrogenation reactions at the metal/oxide interface. *J. Am. Chem. Soc.* **2017**, *139*, 9739−9754.
(17) Studt, F.; Behrens, M.; Kunkes, E. L.; Thomas, N.; Zander, S.; Tarasov, A.; Schumann, J.; Frei, E.; Varley, J. B.; Abild-Pedersen, F.; Nørskov, J. K.; Schlögl, R. The Mechanism of CO and CO_2 Hydrogenation to Methanol over Cu-Based Catalysts. *ChemCatChem* **2015**, *7*, 1105−1111.
(18) Chinchen, G.; Denny, P. J.; Parker, D. G.; Spencer, M. S.; Whan, D. A. Mechanism of methanol synthesis from $CO_2/CO/H_2$ mixtures over copper/zinc oxide/alumina catalysts: use of14C-labelled reactants. *Appl. Catal* **1987**, *30*, 333.
(19) Lunkenbein, T.; Girgsdies, F.; Kandemir, T.; Thomas, N.; Behrens, M.; Schlögl, R.; Frei, E. Bridging the time gap: a copper/zinc oxide/aluminum oxide catalyst for methanol synthesis studied under industrially relevant conditions and time scales. *Angew. Chem., Int. Ed.* **2016**, *55*, 12708−12712.
(20) Hagman, B.; Posada-Borbón, A.; Schaefer, A.; Shipilin, M.; Zhang, C.; Merte, L. R.; Hellman, A.; Lundgren, E.; Grönbeck, H.; Gustafson, J. Steps Control the Dissociation of CO_2 on Cu(100). *J. Am. Chem. Soc.* **2018**, *140*, 12974−12979.
(21) Kasatkin, I.; Kurr, P.; Kniep, B. L.; Trunschke, A.; Schlögl, R. Role of Lattice Strain and Defects in Copper Particles on the Activity of $Cu/ZnO/Al_2O_3$ Catalysts for Methanol Synthesis. *Angew. Chem.* **2007**, *119*, 7465−7468.

(22) Amann, P.; Klötzer, B.; Degerman, D.; Köpfle, N.; Götsch, T.; Lömker, P.; Rameshan, C.; Ploner, K.; Bikaljevic, D.; Wang, H.-Y.; Soldemo, M.; Shipilin, M.; Goodwin, C. M.; Gladh, J.; Halldin Stenlid, J.; Börner, M.; Schlueter, C.; Nilsson, A. The state of zinc in methanol synthesis over a Zn/ZnO/Cu(211) model catalyst. *Science (New York, N. Y.)* **2022**, *376*, 603−608.
(23) Günter, M. M.; Ressler, T.; Bems, B.; Büscher, C.; Genger, T.; Hinrichsen, O.; Muhler, M.; Schlögl, R. Implication of the microstructure of binary Cu/ZnO catalysts for their catalytic activity in methanol synthesis. *Catal. Lett.* **2001**, *71*, 37−44.
(24) Zheng, H.; Gruyters, M.; Pehlke, E.; Berndt, R. "Magic" vicinal zinc oxide surfaces. *Phys. Rev. Lett.* **2013**, *111*, 086101.
(25) Gleißner, R.; Noei, H.; Chung, S.; Semione, G. D. L.; Beck, E. E.; Dippel, A.-C.; Gutowski, O.; Gizer, G.; Vonk, V.; Stierle, A. Copper Nanoparticles with High Index Facets on Basal and Vicinal ZnO Surfaces. *J. Phys. Chem. C* **2021**, *125*, 23561−23569.
(26) van den Berg, R.; Prieto, G.; Korpershoek, G.; van der Wal, L. I.; van Bunningen, A. J.; Lægsgaard-Jørgensen, S.; de Jongh, P. E.; de Jong, K. P. Structure sensitivity of Cu and CuZn catalysts relevant to industrial methanol synthesis. *Nat. Commun.* **2016**, *7*, 13057.
(27) Roy, S. K.; Bose, S. K.; Sircar, S. C. Pressure dependencies of copper oxidation for low- and high-temperature parabolic laws. *Oxidation of Metals* **1991**, *35*, 1−18.
(28) Chen, C.-H.; Yamaguchi, T.; Sugawara, K.-i.; Koga, K. Role of stress in the self-limiting oxidation of copper nanoparticles. *J. Phys. Chem. B* **2005**, *109*, 20669−20672.
(29) Rhodin, T. N. Low Temperature Oxidation of Copper. II. Reaction Rate Anisotropy 1. *J. Am. Chem. Soc.* **1951**, *73*, 3143−3146.
(30) Platzman, I.; Brener, R.; Haick, H.; Tannenbaum, R. Oxidation of Polycrystalline Copper Thin Films at Ambient Conditions. *J. Phys. Chem. C* **2008**, *112*, 1101−1108.
(31) Diaz Leon, J. J.; Fryauf, D. M.; Cormia, R. D.; Zhang, M.-X. M.; Samuels, K.; Williams, R. S.; Kobayashi, N. P. Reflectometry-Ellipsometry Reveals Thickness, Growth Rate, and Phase Composition in Oxidation of Copper. *ACS Appl. Mater. Interfaces* **2016**, *8*, 22337−22344.
(32) Gattinoni, C.; Michaelides, A. Atomistic details of oxide surfaces and surface oxidation: the example of copper and its oxides. *Surf. Sci. Rep.* **2015**, *70*, 424−447.
(33) Dulub, O.; Batzill, M.; Diebold, U. Growth of Copper on Single Crystalline ZnO: Surface Study of a Model Catalyst. *Top. Catal.* **2005**, *36*, 65−76.
(34) Koplitz, L. V.; Dulub, O.; Diebold, U. STM Study of Copper Growth on ZnO(0001)−Zn and ZnO(000$\bar{1}$)−O Surfaces. *J. Phys. Chem. B* **2003**, *107*, 10583−10590.
(35) Stierle, A.; Keller, T. F.; Noei, H.; Vonk, V.; Röhlsberger, R. DESY NanoLab. *Journal of Large-Scale Research Facilities JLSRF* **2016**, *2*, A76.
(36) Schell, N.; King, A.; Beckmann, F.; Fischer, T.; Müller, M.; Schreyer, A. The High Energy Materials Science Beamline (HEMS) at PETRA III. Mechanical Stress Evaluation by Neutrons and Synchrotron Radiation VI. *MSF* **2013**, *772*, 57−61.
(37) Schrode, B.; Pachmajer, S.; Dohr, M.; Röthel, C.; Domke, J.; Fritz, T.; Resel, R.; Werzer, O. GIDVis: a comprehensive software tool for geometry-independent grazing-incidence X-ray diffraction data analysis and pole-figure calculations. *J. Appl. Crystallogr.* **2019**, *52*, 683−689.
(38) WavemMetrics, Lake Oswego, OR, Igor Pro. https://www.wavemetrics.com/.
(39) Vlieg, E. ROD: a program for surface X-ray crystallography. *J. Appl. Crystallogr.* **2000**, *33*, 401−405.
(40) Website of the ANAROD package at the ESRF. 2017; http://www.esrf.eu/computing/scientific/joint_projects/ANA-ROD/.
(41) Stierle, A.; Vlieg, E. Surface-Sensitive X-ray Diffraction Methods. In *Modern Diffraction Methods*; Wiley: 2013.
(42) Stierle, A. fewlay - a software for fitting x-ray reflectivity curves. Information about the software can be obtained from A. Stierle: andreas.stierle@desy.de.
(43) Parratt, L. G. Surface studies of solids by total reflection of X-rays. *Phys. Rev.* **1954**, *95*, 359.
(44) Muntwiler, M.; Zhang, J.; Stania, R.; Matsui, F.; Oberta, P.; Flechsig, U.; Patthey, L.; Quitmann, C.; Glatzel, T.; Widmer, R.; Meyer, E.; Jung, T. A.; Aebi, P.; Fasel, R.; Greber, T. Surface science at the PEARL beamline of the Swiss Light Source. *Journal of Synchrotron Radiation* **2017**, *24*, 354−366.
(45) Schlüter, C.; Gloskovskii, A.; Ederer, K.; Schostak, I.; Piec, S.; Sarkar, I.; Matveyev, Y.; Lömker, P.; Sing, M.; Claessen, R.; Wiemann, C.; Schneider, C. M.; Medjanik, K.; Schönhense, G.; Amann, P.; Nilsson, A.; Drube, W. The new dedicated HAXPES beamline P22 at PETRA III. *AIP Conf. Proc.* **2019**, 040010.
(46) Amann, P.; Degerman, D.; Lee, M.-T.; Alexander, J. D.; Shipilin, M.; Wang, H.-Y.; Cavalca, F.; Weston, M.; Gladh, J.; Blom, M. A high-pressure x-ray photoelectron spectroscopy instrument for studies of industrially relevant catalytic reactions at pressures of several bars. *Rev. Sci. Instrum.* **2019**, *90*, 103102.
(47) Jedrecy, N.; Gallini, S.; Sauvage-Simkin, M.; Pinchaux, R. Copper growth on the O-terminated ZnO(000$\bar{1}$) surface: Structure and morphology. *Phys. Rev. B* **2001**, *64*, 458.
(48) Otte, H. M. Lattice Parameter Determinations with an X−Ray Spectrogoniometer by the Debye−Scherrer Method and the Effect of Specimen Condition. *J. Appl. Phys.* **1961**, *32*, 1536−1546.
(49) Restori, R.; Schwarzenbach, D. Charge density in cuprite, Cu_2O. *Acta Crystallographica Section B Structural Science* **1986**, *42*, 201−208.
(50) Reicho, A.; Stierle, A.; Costina, I.; Dosch, H. Stranski−Krastanov like oxide growth on Ag(111) at atmospheric oxygen pressures. *Surf. Sci.* **2007**, *601*, L19−L23.
(51) Robinson, I. K. Crystal truncation rods and surface roughness. *Phys. Rev. B* **1986**, *33*, 3830−3836.
(52) Batyrev, E. D.; van den Heuvel, J. C. Modification of the ZnO(0001)-Zn surface under reducing conditions. *Phys. Chem. Chem. Phys.* **2011**, *13*, 13127−13134.
(53) Beinik, I.; Hellström, M.; Jensen, T. N.; Broqvist, P.; Lauritsen, J. V. Enhanced wetting of Cu on ZnO by migration of subsurface oxygen vacancies. *Nat. Commun.* **2015**, *6*, 8845.
(54) Mehta, M.; Meier, C. Controlled etching behavior of O-polar and Zn-polar ZnO single crystals. *J. Electrochem. Soc.* **2011**, *158*, H119.
(55) Lunkenbein, T.; Schumann, J.; Behrens, M.; Schlögl, R.; Willinger, M. G. Formation of a ZnO overlayer in industrial Cu/ZnO/Al_2O_3 catalysts induced by strong metal−support interactions. *Angew. Chem.* **2015**, *127*, 4627−4631.
(56) Vegard, L. Die Konstitution der Mischkristalle und die Raumfüllung der Atome. *Zeitschrift für Physik* **1921**, *5*, 17−26.
(57) Grunwaldt, J.-D.; Molenbroek, A.; Topsøe, N.-Y.; Topsøe, H.; Clausen, B. In Situ Investigations of Structural Changes in Cu/ZnO Catalysts. *J. Catal.* **2000**, *194*, 452−460.
(58) Swanson, H. E.; Tatge, E. Standard X-ray diffraction patterns. *Journal of Research of the National Bureau of Standards* **1951**, *46*, 318.
(59) Suh, I.-K.; Ohta, H.; Waseda, Y. High-temperature thermal expansion of six metallic elements measured by dilatation method and X-ray diffraction. *J. Mater. Sci.* **1988**, *23*, 757−760.
(60) Malevu, T.; Ocaya, R. Effect of annealing temperature on structural, morphology and optical properties of ZnO nano-needles prepared by zinc-air cell system method. *Int. J. Electrochem. Sci.* **2015**, *10*, 1752−1761.
(61) Hardi, P. T.; Wibisono, M. Determination of Zn composition of α-brass sing diffraction method: a comparison with Vegard's law. *Proceedings of The International Conference on Materials Science and Technology*. **2010**.
(62) Beck, A.; Zabilskiy, M.; Newton, M. A.; Safonova, O.; Willinger, M. G.; van Bokhoven, J. A. Following the structure of copper-zinc-alumina across the pressure gap in carbon dioxide hydrogenation. *Nature Catalysis* **2021**, *4*, 488−497.
(63) Yang, Y.; Mims, C. A.; Mei, D.; Peden, C. H.; Campbell, C. T. Mechanistic studies of methanol synthesis over Cu from CO/CO_2/

https://doi.org/10.1021/acsanm.3c01306
ACS Appl. Nano Mater. 2023, 6, 8004−8016

H_2/H_2O mixtures: The source of C in methanol and the role of water. *Journal of Catalysis* **2013**, *298*, 10−17.
(64) Pielsticker, L.; Nicholls, R.; Beeg, S.; Hartwig, C.; Klihm, G.; Schlögl, R.; Tougaard, S.; Greiner, M. Inelastic electron scattering by the gas phase in near ambient pressure XPS measurements. *Surf. Interface Anal.* **2021**, *53*, 605−617.
(65) Eren, B.; Zherebetskyy, D.; Patera, L. L.; Wu, C. H.; Bluhm, H.; Africh, C.; Wang, L.-W.; Somorjai, G. A.; Salmeron, M. Activation of Cu (111) surface by decomposition into nanoclusters driven by CO adsorption. *Science* **2016**, *351*, 475−478.
(66) Roiaz, M.; Falivene, L.; Rameshan, C.; Cavallo, L.; Kozlov, S. M.; Rupprechter, G. Roughening of copper (100) at elevated CO pressure: Cu adatom and cluster formation enable CO dissociation. *J. Phys. Chem. C* **2019**, *123*, 8112−8121.
(67) Setvín, M.; Daniel, B.; Mansfeldova, V.; Kavan, L.; Scheiber, P.; Fidler, M.; Schmid, M.; Diebold, U. Surface preparation of TiO_2 anatase (101): Pitfalls and how to avoid them. *Surf. Sci.* **2014**, *626*, 61−67.
(68) Bao, H.; Zhang, W.; Shang, D.; Hua, Q.; Ma, Y.; Jiang, Z.; Yang, J.; Huang, W. Shape-Dependent Reducibility of Cuprous Oxide Nanocrystals. *J. Phys. Chem. C* **2010**, *114*, 6676−6680.
(69) Amann, P.; Klötzer, B.; Degerman, D.; Köpfle, N.; Götsch, T.; Lömker, P.; Rameshan, C.; Ploner, K.; Bikaljevic, D.; Wang, H.-Y.; et al. The state of zinc in methanol synthesis over a Zn/ZnO/Cu (211) model catalyst. *Science* **2022**, *376*, 603−608.
(70) Gleißner, R.; Beck, E. E.; Chung, S.; Semione, G. D. L.; Mukharamova, N.; Gizer, G.; Pistidda, C.; Renner, D.; Noei, H.; Vonk, V.; Stierle, A. Operando reaction cell for high energy surface sensitive x-ray diffraction and reflectometry. *Rev. Sci. Instrum.* **2022**, *93*, 073902.

https://doi.org/10.1021/acsanm.3c01306
ACS Appl. Nano Mater. 2023, 6, 8004−8016